CASE STUDY
doi:10.59236/geomorphica.v2i2.58

GEOMORPHICA

Hydrothermal processes influence the along-strike morphologic variability of fault scarp profiles: applying supervised machine learning to Holocene scarps in the Stillwater Seismic Gap, Dixie Valley, Nevada, USA

Cassandra A.P. Brigham * [1,2], **Owen A. Callahan** [1,3], **Juliet G. Crider** [1]

[1]Department of Earth and Space Sciences, University of Washington, Seattle, USA, [2]School of Earth and Space Exploration, Arizona State University, Tempe, Arizona, USA, [3]En Échelon Geosolutions, Palo Alto, California, USA

Author contributions: *Conceptualization*: C. Brigham, O. Callahan. *Investigation*: C. Brigham, O. Callahan. *Formal analysis*: C. Brigham. *Writing - original draft*: C. Brigham, O. Callahan, J. Crider. *Review & editing*: C. Brigham, O. Callahan, J. Crider. *Funding acquisition*: O. Callahan, J. Crider.

Abstract Fault scarp morphology can yield information about the age and slip distribution of surface-rupturing earthquakes. However, bedrock characteristics and geomorphic modification also contribute to scarp form. Additional complications arise in settings where hydrothermal processes modify the material properties of the faulted surface material. We present a case study where a single Holocene scarp offsets three adjacent units: alluvial and colluvial gravels; quartz-rich sinter and silicified gravels; and clay-rich, acid-sulfate-altered gravels and bedrock. We examined scarp-normal topographic profiles in each unit and employed supervised machine learning to describe the variations in scarp form and quantify changes in morphologic variability. In the alluvial and colluvial deposits, scarp profiles have a mean height of 6.2 ($\pm$ 0.9) m and exhibit low morphologic variability. The section of the scarp through hot spring sinter and cemented gravels has a mean height of 5.8 ($\pm$ 0.8) m and exhibits a high degree of along-strike variability. In the altered section NM1.1, the individual Holocene scarp is difficult to discern and has low morphologic variability. Our study emphasizes the need to consider fault scarp composition during paleoseismic interpretation, and illustrates the potential utility of along-strike fault scarp morphologic variability in identifying lithologic and paleohydraulic boundaries.

Non-technical summary Fault scarps are steps in the landscape that hold a record of earthquake-related fault slip. The shape of a fault scarp in profile changes with time: older scarps have experienced more erosion and typically have a more rounded form. However, the change in shape of the scarp with time depends on the material that is being eroded. In this study, we examine a single fault scarp that crosses three different geologic materials, enabling a direct comparison: loose gravels, gravels that have been cemented by hot spring minerals, and bedrock and gravels that have been modified by geothermal processes. We used drone photographs to produce high-resolution topographic models of the landscape and an original automated computer classification tool to identify sections of the fault scarp with different profile shapes. We find that the cemented gravels (likely the strongest material) show greater variation in scarp shape than the loose gravels, and that the altered bedrock and gravels (likely the weakest materials) show low variation in scarp shape. Our approach shows that scarp shape can help identify a change in rock type and trace the influence of hot spring fluids in persistence or erosion of landforms.

Received: August 25, 2025
Accepted: May 12, 2026
Published: Jul 8, 2026

Editor-in-Chief: Alice Lefebvre
Associate Editors: Anonymous
Managing Editor: Nathaniel Klema
Copy Editor: Nari Miller
Production Editor: Leo Guerrero

Reviewers: Anonymous

Introduction

Fault scarps are steps in the landscape created by surface-rupturing faults. Fault scarp morphology is influenced by fault slip, rock properties, and geomorphic processes. Quantitative descriptions of scarp morphology are used to model seismic hazard (e.g., Zou et al. (2022)), fault zone structure and age (e.g., Sare et al. (2019)) and rates of geomorphic processes (e.g., Tucker et al. (2011)). Traditional scarp degradation models focus on diffusion-based erosion processes and commonly assume uniform lithology, climate, and material properties along a given scarp (e.g., Wallace (1977); Bucknam and Anderson (1979); Nash (1980); Hanks (2000)). These models typically analyze single scarp profiles or use individual morphologic metrics (e.g., slope or curvature) to estimate scarp age. However, fault scarps can exhibit significant along-strike variability in form, particularly in jointed bedrock (e.g. Brigham and Crider (2022)), reflecting lateral differences in scarp characteristics such as coseismic slip variability, rock mass characteristics, fault structures, or degree of geomorphic modification, rather than just age-dependent degradation.

Additional complications arise in fault zones hosting hydrothermal systems, where hydrothermal processes leading to chemical alteration and mineral precipita-

*Corresponding author: criderj@uw.edu

tion which may modify the properties of the host materials before or after rupture. In exhumed fault zones, Callahan et al. (2019) demonstrated that the accumulation of fault zone damage versus degree of annealing by mineral cementation influences bulk rock strength and fracture toughness in hydrothermal systems. In shallow epithermal settings dominated by rapid accumulation of hydrothermal quartz, strength contrasts between the fault damage zone and mineralized fault core contribute to strong, thick fault cores prone to brittle dilation (Caine et al., 2010; Callahan et al., 2020). Alternatively, clay and dissolution-dominated alteration contributes to rock weakening (Wintsch et al., 1995; Pola et al., 2014; Wyering et al., 2014; Heap et al., 2015; Backeberg et al., 2016), which is particularly pronounced in acid-sulfate (fumarole, or advanced argillic alteration) settings and may influence the strength and stability of volcanic edifices and other hydrothermal landforms (Reid et al., 2001; Pereira et al., 2024). In extreme settings, active hydrothermal processes may grow surface landforms through the accumulation of precipitated minerals in large mounds and terraces, or modify them by hydrothermal eruptions (e.g. White (1955); Browne and Lawless (2001); Yellowstone Volcano Observatory (2026).

Characterizing scarp morphology quantitatively in these complex conditions requires an approach that considers the along-strike variation in scarp morphology and the influence of diverse processes. Brigham and Crider (2022) developed an algorithm to quantify along-strike variations in scarp form, through semi-automatic classification of typical scarp profile forms and calculation of a morphologic variability metric, which measures the number and proportion of form classes in a moving window along a linear landform. This method has a geologist define morphologic classes and construct a representative training dataset for each class, then employs a supervised learning algorithm to automatically classify unlabeled profiles by proximity to the labeled data. Because this approach uses expert knowledge to define different classes, it is grounded in a geological interpretation, with classes that are defined by the features of the particular system under study.

We present a case study based on the morphologic variability method of Brigham and Crider (2022) from Dixie Valley, Nevada, where three distinct surface materials along a 2.5 km section are offset by a single, continuous Holocene fault rupture. The adjacent units are: alluvial and colluvial gravels; quartz-rich hot spring sinter and silicified gravels; and variably clay-altered and cemented gravels and footwall rock in a zone of ongoing fumarole activity. The scarp is in the Stillwater Seismic Gap segment of the Dixie Valley fault, named due to its location between coseismic surface ruptures of the 1915 Pleasant Valley earthquake to the north and 1954 Fairview Peak-Dixie Valley earthquake sequence to the south (Wallace and Whitney, 1984). This site provides the opportunity to apply the morphologic variability metric to a scarp where age and climate are constant, but where hydrothermal processes have altered lithologic characteristics along the scarp. Our goal is to document the morphologies present along the fault scarp in these three units using high resolution topographic datasets and to quantify the degree of variation in scarp profile. If all units have similar morphologic variability values, the variation in profile form can be attributed to fault zone-scale attributes (e.g., primary fault structure). However, if each unit exhibits distinct morphologic variability values, this indicates that lithologic differences are the primary driver of scarp form. In this study, we show that scarp segments affected by hydrothermal processes have markedly different morphologic characteristics than those in unaltered gravels, illustrating how hydrothermal history leaves a measurable geomorphic signature along faults.

The ability to infer lithologic changes from scarp morphology also has important implications for remotely sensed geothermal exploration. Active and extinct geothermal systems modify fault zone rocks through mineralization, dissolution, and alteration, creating sharp contrasts in material properties along faults. Our findings suggest that analyzing fault scarp morphologic variability provides a new tool for identifying lithologic boundaries, including those associated with hydrothermal modification, remotely.

Geologic Setting

The Dixie Valley fault is a range-front normal fault that bounds the east side of the Stillwater Range in western Nevada, United States (Fig. 1). The Stillwater Seismic Gap is situated in the northern section of the Dixie Valley fault and separates sets of fault scarps formed during the 1915 Pleasant Valley earthquake from scarps formed during the 1954 Dixie Valley earthquake (Wallace and Whitney, 1984). Though there are no historical surface ruptures identified in the Stillwater Seismic Gap, a series of discontinuous fault scarps are present along this section. Trench studies, radiocarbon ages and morphometric analyses of scarp profiles obtained in the gap indicate that these scarps were likely formed during a single Holocene event (the "Gap Event") that occurred between 2 and 2.5 ka (Caskey, 2002; Lutz et al., 2003). Vertical offset across the scarps in this section average 2–3 m, up to 7 m. Paleoseismic investigations indicate that these scarps represent the only surface rupture along the range front in the last 12 ky, with the Gap Event constrained to between 2.0 and 2.5 ka (Caskey, 2002; Wesnousky et al., 2003; Lutz et al., 2003). Based on rupture length and average slip estimates, the moment magnitude of the Gap Event earthquake is estimated to be about Mw 7.3 (Wesnousky et al., 2003).

The field site includes the Holocene fault scarps and ongoing hydrothermal alteration within the Stillwater Seismic Gap. Scarps in this region transect alluvium, alluvium capped by and cemented with centimeter-to-decimeter-thick layers of siliceous sinter and geyserite, and a region modified by ongoing hydrothermal activity. Alluvial-fan and colluvial deposits partially bury older beach gravels deposited during the high stand of pluvial Lake Dixie, dating to approximately 13–14 ka BP (Thompson and Burke, 1973), and predate the approximately 1.5 ka Mono Crater ash (Bell, 1981; Bell and Katzer, 1990). These deposits are composed of sandy pebble-to-cobble gravel and gravelly sand and represent many discrete water-flood and debris-flow events, as well as rockfall and shallow slides from the steep rangefront (Bell and Katzer, 1990). Northeast of the fault section in alluvium, the scarp traverses extinct Holocene sinter deposits, or geyserite, emanating from fault splays along the rangefront escarpment. The deposits indicate the former presence of high-temperature hot spring vents (Lutz et al., 2002). At the base of the geyserite, interbedded sinter and stream cobbles, along with silica-cemented gravels, create terraces of resistant material, dating to approximately 3.4–2.5 ka (Lutz et al., 2002). Further northeast, the fault traverses a region of ongoing weak fumarole activity and steaming ground referred to as the Section 10/15 fumaroles and sinter (Lutz et al., 2002), and known colloquially as the "Frying Pan" fumaroles. Hydrothermal activity in this region manifests as weak fumaroles with temperatures to 95 °C, zones of damp red clay and gypsum, warm, dry ground associated with vegetation anomalies, and variably altered footwall bedrock. Unusual alluvial fan-head morphology in the fumarole area is attributed to a series of possible hydrothermal explosion craters (M. Coolbaugh, personal communication). Weak fumarolic activity is ongoing, but initial alteration of this area began approximately at 5 ka (Lutz et al., 2002). The 2–2.5 ka scarp transects the altered zone, but is difficult to trace in its entirety.

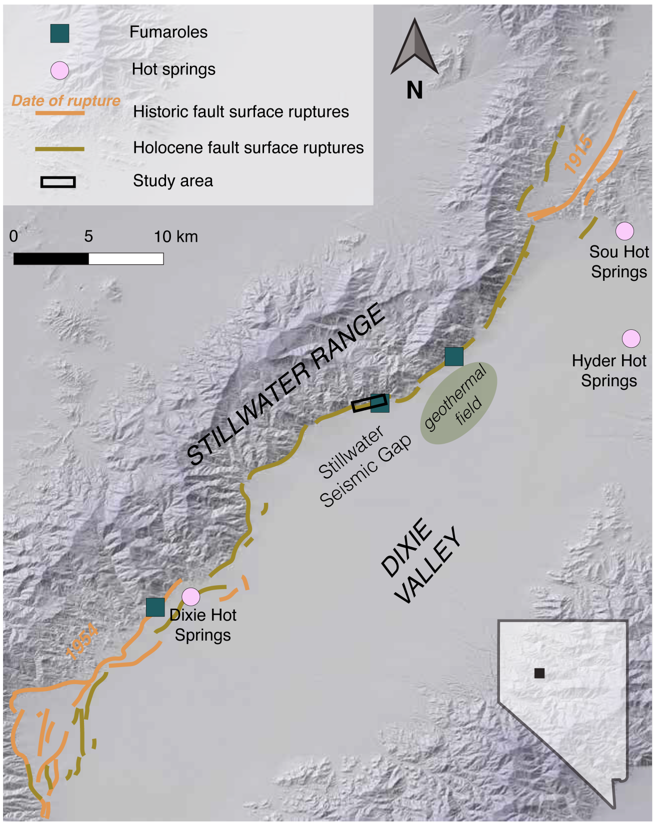

Figure 1 Map of study site at the base of the Stillwater Range. Inset shows location in Nevada. Orange lines indicate the traces of surface ruptures from the 1915 and 1954 earthquakes, khaki traces indicate older Holocene ruptures. Black box shows study area and location of SfM survey. Hydrothermal features and scarps are from Lutz et al. (2002); Callahan et al. (2019).

Methods

Structure-from-Motion photogrammetry and field mapping

We collected UAV aerial imagery for use in Structure-from-Motion photogrammetry (Westoby et al., 2012). We used Agisoft Metashape to match features between 2429 images featuring 5 GNSS-surveyed ground control points to create a three-dimensional model of the field site and derived products, such as a 1.5 cm^2/pixel resolution orthorectified image and a 6 cm^2/pixel resolution digital elevation model (DEM) of our study area (see details in Callahan et al. (2023); data available from OpenTopography). We made field observations of fault morphology, faulted materials, and hydrothermal alteration and activity, and mapped the fault scarp trace and the hydrothermal features onto our SfM-derived DEM (Fig. 2).

Quantitative analysis of morphologic variability

To quantitatively determine the degree to which profile form varies in each section, we use a morphologic variability metric derived from a supervised machine learning workflow that integrates expert knowledge with statistical learning algorithms (Brigham and Crider, 2022). First, we examined a sub-sample of profiles taken perpendicular to the scarp and defined morphologic classes based on common profile shapes (e.g. profiles with a pronounced steep upper slope versus those with a more rounded form, etc.). We then created a training dataset (10–50 profiles per class; see Fig. 3) by labeling the sampled profiles according to their class. This step injects domain knowledge, ensuring that the classes are rooted in geologic observations. Our method does not rely on predefined morphometric indices (such as those based on slope or curvature of the whole profile) for classification, but rather uses the full shape of the scarp cross-sectional profile as the input for the classification step of the analysis. Each scarp profile is automatically cropped to the scarp toe and crest (curvature is used in a preprocessing step to identify the crest of and toe of a scarp) and normalized by the scarp height, and the processed profile coordinates form the basis of the classification (see Brigham and Crider (2022), equation 2 for normalization details).

Each normalized scarp profile consists of many coordinate pairs. Principal component analysis (PCA, implemented via singular value decomposition) is applied to the collection of profiles to identify dominant morphologic traits and reduce the data to a few principal components suitable for classification. Using the principal component scores of the profiles as input features, we train a support vector machine (SVM) classifier. The SVM is a supervised learning algorithm well-suited for smaller datasets; it finds the optimal boundaries in the multi-dimensional feature space that separate the classes. The SVM model, once trained, can predict the class of new, unlabeled profiles. Once the scarp profiles are classified, we compute the morphologic variability of the scarp from the number of different morphologic

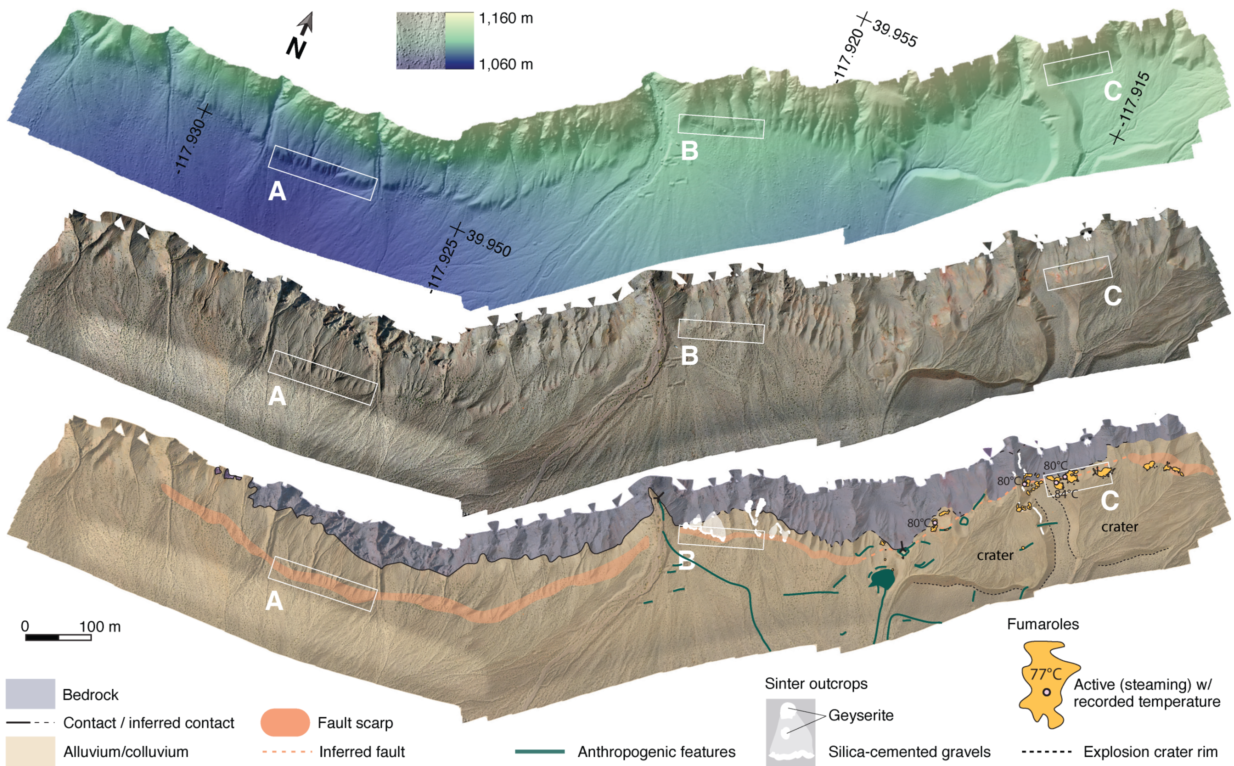

Figure 2 Maps of the study area. Upper panel: structure-from-motion-generated hillshade colored by elevation. Central panel: orthorectified UAV photomosaic. Lower panel: geologic map. White rectangular boxes indicate where scarp profiles were extracted in the alluvial fan/colluvial deposits (Section A); in the sinter and silica-cemented deposits (Section B); in the fumarole area (Section C). Geologic map created by the authors based on field observations and SfM imagery interpretation.

classes represented in a sliding window along the scarp and the statistical distribution of those classes (specifically, the standard deviation of their proportions). This sliding-window analysis turns the sequence of classified profiles into a continuous variability profile along the scarp. Further details of our methodology are described in Brigham and Crider (2022).

To apply the morphological variability metric to the scarps of the Stillwater Seismic Gap, we extract scarp-normal profiles from the SfM-derived DEM in each of the three faulted lithologies (gravel, cemented, and altered). For each area, we sampled profiles from a section (areas A, B and C in Fig. 2) where the scarp location is known and where profile morphology is not noticeably affected by the rangefront alluvial channels or by anthropogenic modification. To calculate the morphologic variability metric, we extracted 289 profiles at a 2-meter spacing in sections representing each of the lithologic units (164 profiles in section A, 53 profiles in section B, 72 profiles in section C). We pre-processed and classified the profiles from each section into our chosen morphologic classes using the SVM method described above. We then calculate the proportion of each class (pclass; ranging from 0 to 1) within a given window along the scarp (Fig. 3), and the standard deviation (σprop) from the mean (μprop) of these proportions. We also determine the number of classes (Nclasses) represented in that window. We thus obtain the scarp variability metric, vs:

$$v_s = \frac{\sum(p_{\text{class}} - \mu_{\text{prop}})^2}{N_{\text{total classes}}} + \frac{N_{\text{classes}}}{N^*_{\text{total classes}}} \tag{1}$$

The metric is normalized, so that 1 represents a landform section that has all classes in equal proportions and 0 is assigned to a scarp section with a single morphologic class. To compare the scarp sections to one another, we use the mean morphologic variability of each section as a representative metric, following Brigham and Crider (2022).

Results

Description of scarp form in each lithologic unit

The fault scarp shows distinct combinations of profile forms in each of the three fault sections influenced by different hydrothermal processes.

Alluvial and colluvial gravels

The Holocene fault scarp is the most easily discernible in the westernmost portion of the study area (section A), in the range-derived alluvial and colluvial gravels and gravelly sand. Scarp profiles in this section have a mean height of 6.2 m (±0.9 m; 1 standard deviation across all height measurements), and scarp faces have an average slope 27.4° (±8.7°). In many areas, the slope takes on a familiar shape for scarps in unconsolidated material: rounded crest and toe, with a straight mid slope (Fig. 4a.i). However, the high degree of fluvial dissection along the range front is apparent in the scarp profile morphology, where the traditional fault scarp shape is sometimes replaced with concave upwards slopes formed by gullying (Fig. 4a.ii) and profiles cross-cut by channels (Fig. 4a.iii).

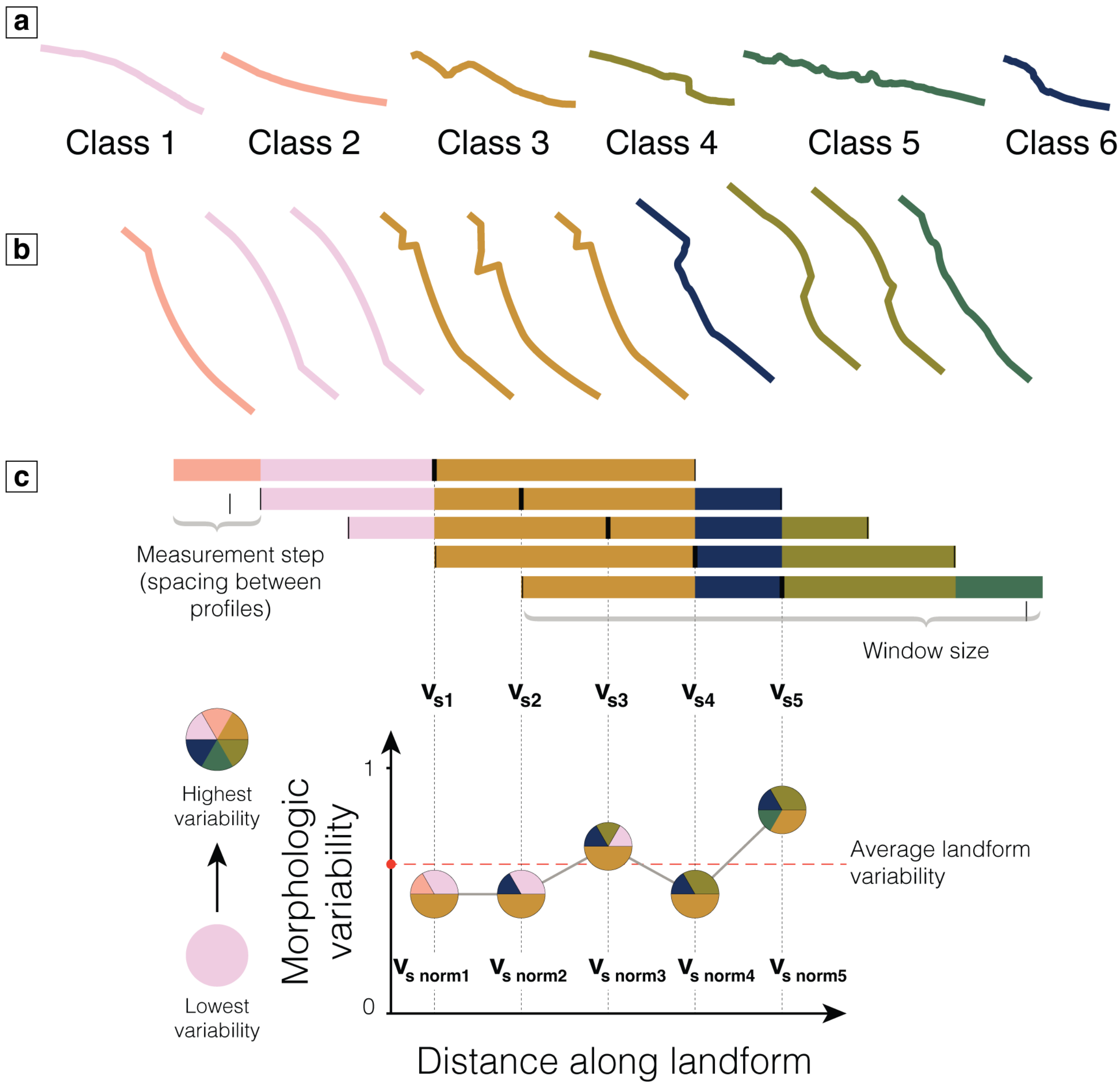

Figure 3 a) Morphologic classes determined by inspection of scarp-normal profiles taken from each unit (profile view) b) Example of possible arrangement of profiles of different morphologic classes along a section of scarp (map view). c) Schematic illustration of how morphologic variability (vs)[NM1.1] is measured in a moving window along the scarp section (modified from Brigham and Crider (2022)).

Sinter and silica cemented gravels

Large sinter deposits characterize the central portion of the study area (section B) in the form of geyserite, a form of silica found in high-temperature hot spring systems. Near the base of the geyserite, we find aprons of silica-cemented gravel that are cut by the Holocene scarp. Scarp profiles in the silicified section have a mean height of 5.8 m (±0.8 m), with an average slope of 23.2° (±10.2°). Depending on the level of cementation, the scarp takes a range of forms: an armored convex-upwards upper slope with a free face in the lower slope (Fig. 4b.i); a convex-upward slope (Fig. 4b.ii); or a slope with short-scale heterogeneities introduced by rubble from collapse of the cemented apron (Fig. 4b.iii).

Altered bedrock and gravels

The eastern portion of the study area (section C) is characterized by outcrops of variably clay-altered and fractured footwall bedrock and cemented gravels in a zone of ongoing fumarole activity. We mapped active, recent, and inactive fumaroles through ground and drone-based temperature measurements, vegetation, and coloration. The fumarolic activity along the fault complicates its surface expression in the alteration zone. The scarp slope relaxes until it reaches a change in lithology, creating a fault line scarp (Fig. 4c.i) or is assimilated into the larger hillslope (Fig. 4c.ii). In the initial stage of profile extraction, we supplemented the curvature-based algorithm to determine the crest and toe with field observations and manual verification.

Morphologic variability analysis

Through detailed field observations and morphometric analyses, we have quantified the variations in profile shape along three sections of a single-age Holocene fault scarp that cuts in Dixie Valley, Nevada. Because the scarp was generated during one rupture event, its

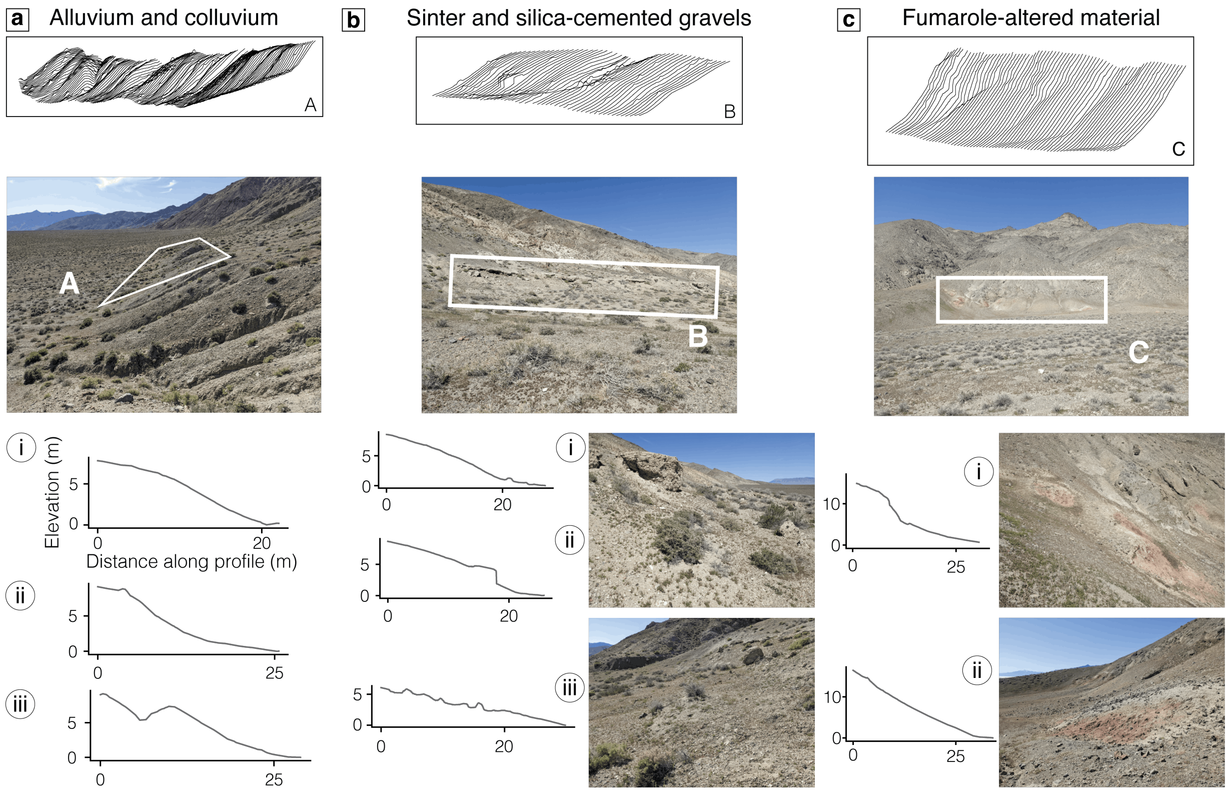

Figure 4 Extracted scarp-normal topographic profiles, photographs of scarps in each study segment and representative examples (i – iii) of scarp-normal topographic profiles illustrating the types of morphologies found in a) alluvial fan and colluvial material; b) sinter and silica-cemented gravels; c) fumarole-altered material. All profiles indicate distance along the scarp in meters on the x-axis and height in meters on the y-axis.

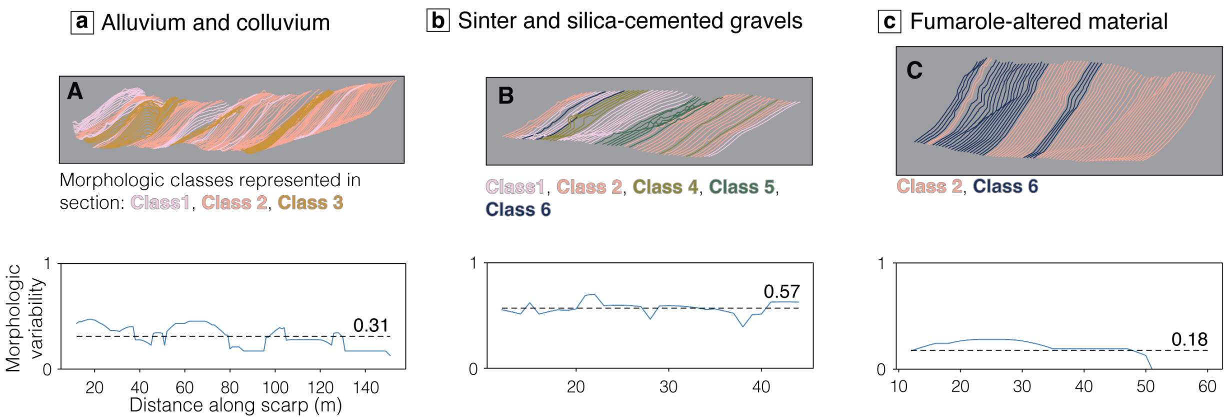

Figure 5. Profiles colored by morphologic class (upper panels) and morphologic variability calculated along scarp section with mean morphologic variability value (lower panels) for: a) alluvial fan and colluvial material; b) sinter and silica-cemented gravels and c) fumarole-altered area.

Figure 5 Profiles colored by morphologic class (upper panels) and morphologic variability calculated along scarp section with mean morphologic variability value (lower panels) for: a) alluvial fan and colluvial material; b) sinter and silica-cemented gravels and c) fumarole-altered area.

age is constant along strike. Regardless of whether the scarp represents a single event or multiple closely-spaced ruptures, all three sections we examined experienced the same rupture history. Therefore, the distinct morphologic variability values we document for each section cannot be attributed to differences in rupture history and must reflect differences in material properties and post-rupture geomorphic processes. This unique circumstance allows us to directly link observed variations in scarp morphology to differences in rock properties and processes rather than to differences in age. Consequently, the distinct mean morphologic variability values we document for alluvial-colluvial gravels, quartz-rich hot spring sinter with silicified gravels, and the clay-rich, hydrothermally-altered area indicate that hydrothermal processes and their subsequent lithologic changes are the primary drivers of along-strike variation in Holocene scarp form in the Stillwater Seismic Gap.

Geomorphic and hydrothermal processes influencing scarp form

The morphologic expression of a fault scarp reflects not only its rupture history, but also the material properties and geomorphic processes that govern its post-rupture evolution. In geothermally active areas like the Stillwater Seismic Gap, hydrothermal processes (e.g., mineral precipitation and chemical alteration) can substantially alter the composition, erodibility, and strength of the faulted materials. These transformations impose a strong control on scarp degradation processes and, in turn, on how we might interpret rupture history from scarp form.

In unaltered and unconsolidated materials like alluvial and colluvial gravels, scarp degradation follows classic diffusion-based hillslope models, as originally described by Culling (1960, 1963) and applied in scarp morphologic dating studies by Wallace (1977); Hanks et al. (1984); Andrews and Hanks (1985). In these materials, sediment transport processes such as rainsplash, sheetwash, and soil creep act on a fresh scarp in a slope-dependent and spatially uniform manner, resulting in characteristic scarp profiles with increasingly rounded, convex-upward crests, linear midslopes, and concave-upward toes. In the unaltered gravel section of the Gap Event scarp, the convex upward type 1 profiles are likely a result of these diffusive processes. The concave upward type 2 profiles either reflect areas where these diffusive processes are not as strong (e.g., due to aspect and microclimate, as shown by Pierce and Colman (1986)), or areas where a secondary process is more dominant. Fluvial dissection along scarps adjacent to ephemeral channels overprint the diffusion signal and create type 3 profiles. Incision creates V-shaped discontinuities or removes the toe entirely, increasing local morphologic variability. Fluvial dissection changed scarp form; if not recognized, such modification might lead to misidentification of the crest of the scarp and underestimation of scarp height (and thus fault throw). These localized overprints illustrate that site selection is critical when using scarp morphology to infer rupture history, even in otherwise predictable materials.

Where the fault scarp cuts hot spring sinter and silica-cemented gravels, the degradation processes shift from uniform hillslope diffusion to heterogeneous and threshold-controlled processes. In some places, geyserite and sinter crusts armor the slope, preserving steep scarps where erosion is inhibited. In other locations, sinter has fractured and collapsed, producing rough, jagged forms with high microtopographic relief. The resulting profile morphologies range from smooth convex-upward forms to multi-tiered scarps with vertical free faces. These forms are difficult to model using linear or nonlinear diffusion (e.g., Andrews and Bucknam (1987); Xu et al. (2021)), because the underlying transport processes are stochastic and spatially variable, involving block toppling, other types of localized failure, or nonlocal sediment transport (as explored by Tucker and Bradley (2010)). The high morphologic variability observed in these segments aligns with findings from jointed bedrock scarps, where lateral variability in material strength or bedrock structure produces significant heterogeneity in profile form (Brigham and Crider, 2022). While sinter-capped scarps tend to accurately record fault offset, the removal of blocks of cemented material and their accumulation at the base of the scarp can inhibit automated identification of the scarp crest and toe. Misinterpretation of these features could lead to underestimation of throw.

In the eastern portion of the study site, the fault crosses areas of relict hydrothermal alteration and ongoing fumarole activity, where the gravels and bedrock have been variably altered into more erodible material. This zone exhibits the lowest morphologic variability, since rapid erosion has homogenized or erased the original scarp form. Scarp slopes have relaxed into the background hillslope or terminate abruptly at lithologic boundaries, creating fault-line scarps where altered material meets a more competent unit. Where the scarp is no longer discernible, we risk underestimating slip or missing rupture evidence entirely. Alternatively, if a lithologic step or degraded slope is mistakenly interpreted as a scarp, overestimation is possible.

The chronology of hydrothermal activity relative to the Gap Event rupture differs between sections. In section B, radiocarbon dating indicates that the sinter deposits formed between approximately 3.4 and 2.5 ka (Lutz et al., 2002, 2003). The sinter terrace is broken and vertically offset by approximately 3–5 meters by the Gap Event fault, demonstrating that sinter formation predates the rupture (Lutz et al., 2003). The silicified material thus records pre-rupture cementation, and post-rupture degradation is expressed through block toppling and collapse of the cemented apron. In section C ((Fig. 2)), fumarolic alteration began approximately 5 ka Lutz et al. (2002) and continues today. The scarp in this section has experienced both syn- and post-rupture alteration, with ongoing acid-sulfate processes weakening materials and promoting rapid erosion. The visible color changes and alteration patterns in section C represent in situ vadose zone alteration rather than tilted former geothermal pools; this type of alteration forms in place within the unsaturated zone where steam and gases rise from depth and condense. Distinguishing the relative contributions of formation versus degradation processes remains challenging, but the contrasting morphologic variability values suggest that material properties at the time of rupture (whether strengthened by cementation or weakened by alteration) exert a primary control on subsequent scarp evolution.

Across all three sections, our observations demonstrate that hydrothermal processes impart distinct geomorphic signatures on fault scarps. These signatures directly impact our ability to infer rupture history from scarp profile form. Segments capped by resistant sinter may appear anomalously fresh and steep, potentially suggesting a much younger scarp age, while segments in easily erodible altered materials degrade rapidly, obscuring evidence of recent faulting.

Many morphologic dating techniques rely on matching observed scarp profiles to diffusion-based models (e.g., Andrews and Bucknam (1987); Avouac (1993); Pelletier et al. (2006)). These models assume uniform diffusivity, consistent initial scarp form, and spatially invariant process rates, assumptions violated in our scenario and in many hydrothermally active areas. Wide-scale, template-matching methods like those of Sare et al. (2019) assume that all scarp forms evolve by linear diffusion, and thus may fail to detect scarps that deviate from the idealized error-function shape, as is the case in our study. This is where tools like the morphologic variability metric developed by Brigham and Crider (2022) become valuable. Rather than assuming a fixed model, the morphologic variability approach uses shape-based classification of scarp profiles to identify areas of variable form, which may reflect changes in material properties, geomorphic processes, or structural complexity along the fault. High variability suggests lateral shifts in material strength or post-rupture modification, while low variability may indicate uniform degradation or, alternatively, complete erosion in highly altered zones. Tracking morphologic variability does not require assumptions about geomorphic processes; however, it also cannot distinguish among different types of geomorphic processes. Instead, clear changes in morphologic variability over short distances along a single fault scarp coincide with mappable distinctions in material properties, which suggest different erosive properties at work. This case study thus addresses the influence of material properties on form patterns rather than identifying specific properties. The approach allows a more flexible machine-learning-based form classification and quantification, useful for heterogeneous terrains.

Application of morphometric variability: remote sensing of scarps and hydrothermal features

Remote sensing has revolutionized the detection and characterization of fault scarps. Many efforts in automated scarp detection focus on mapping topographic discontinuities from high-resolution DEMs (e.g., Wolfe et al. (2020); Vega-Ramírez et al. (2021); Scott et al. (2022)), using methods such as slope and curvature filtering, as well as analyses of other geomorphic indices to filter out other linear features. Machine learning methods using multi-modal remote sensing data (topography and satellite or UAV imagery) and deep learning approaches (e.g., Juliani (2019); Hermant et al. (2025)) are the latest advancement in detection algorithms. Other methodologies venture beyond detection and seek to characterize the morphologic age of fault scarps. Hodge et al. (2019) developed a semi-automated method to extract scarp profiles and fit them with diffusion-based models to infer morphologic age. Sare et al. (2019) extended this further to regional-scale mapping by comparing extracted scarp profiles with idealized diffusion model templates. While powerful in the correct conditions (see section 5.1.), these methods assume that all scarps evolve through linear or nonlinear diffusion and may struggle to interpret scarps in bedrock or forms modified by lithologic or hydrothermal complexities. In contrast, Brigham and Crider (2022) use high-resolution remotely sensed topographic data to detect and quantitatively describe the variations of along-strike morphology of fault scarps in any medium. Brigham and Crider (2022) investigated morphologic variability changes with scarp age and showed that morphologic variability of fault scarps decreases with age for a single lithology (jointed basalt). Herein, we show how the morphologic variability metric allows us to use remote sensing methods to gather information about the changes in lithology and process along a single-age linear landform. Thanks to advances in machine learning methods, gathering datasets to compare against morphologic variability can become increasingly automated and remotely sensed. For example, Chen et al. (2023) trained a convolutional neural network to quantify the number and orientation of blocks in the talus slopes of fractured bedrock fault scarps, an important indicator of process.

Remote sensing has also become integral to geothermal exploration. Numerous studies have demonstrated the effectiveness of satellite-based methods to identify surface expressions of geothermal activity through alteration minerals, vegetation stress, and thermal anomalies, including studies in the broader Dixie Valley region (Kennedy-Bowdoin et al., 2003; Martini et al., 2004). Van Der Meer et al. (2014); Kraal and Schwering (2024) outline how multispectral and hyperspectral imagery can detect key hydrothermal minerals such as opal, kaolinite, alunite, and illite associated with fumarolic and sinter-forming systems. Shebl et al. (2023) showed that combining ASTER, Sentinel-2, and Landsat-8 with airborne geophysical data (e.g., magnetic data) enhances delineation of hydrothermal zones. Freski et al. (2021) demonstrated that lidar laser return intensity could discriminate degrees of alteration even beneath vegetation. Similarly, Rahmidiani et al. (2025) used vegetation response indices (e.g., red-edge vegetation index) to identify stress related to subsurface hydrothermal circulation, showing that vegetation itself can act as a geothermal indicator. Together, these methods offer a robust toolkit for geothermal reconnaissance. However, most focus on identifying individual spectral indicators, which rely on surface reflectance, or geophysical data, and might require specific flight campaigns. The morphologic variability metric offers a complementary method that requires only high-resolution topographic data and can map boundaries of hydrothermally-modified zones. By computing a shape-based variability metric, we provide a novel structural and geomorphic proxy for identifying hydrothermal zones in areas with fault scarps.

Classifying landforms with a geologist-informed algorithm

Our use of the morphologic variability metric builds on the understanding that landform classification in tectonically and lithologically complex regions benefits from expert interpretation and flexible, data-efficient methods (Brigham and Crider, 2022). This semi-automated, human-in-the-loop approach enables geologists to define shape-based morphologic classes grounded in field observations and process-based hypotheses. These are then used to train a supervised SVM classifier, making the classification and subsequent variability computation transparent and reproducible.

This framework offers several advantages over fully automated classification in terms of interpretability, adaptability, and data efficiency. Expert-defined, shape-based profile classes are directly tied to observable geomorphic forms, unlike abstract features extracted by convolutional neural networks (CNNs) or transformer models. The method also captures whole-profile geometry rather than relying solely on scalar metrics (such as slope or curvature) that require more post-classification interpretation. In this manner, the morphologic variability metric bridges classic geomorphometry and semantic segmentation (Xiong et al., 2022). The morphologic variability method is adaptable to new sites or landform types, since new morphological types can be added without retraining a large model. Appropriate landform types include linear landforms with defined start and end points along cross-sectional profiles such as terrace risers, shoreline and paleo-shoreline scarps, levees, coastal cliffs, moraine crests and volcanic fissure scarps. The algorithm uses matrix operations efficiently and performs well with both small (100 profiles) and large (>10k profiles) datasets. Most importantly, the morphologic variability metric reveals patterns in landform complexity that reflect underlying geological characteristics or processes, helping delineate lithologic transitions, altered zones, or structural complexity. In our study, we demonstrate that scarp form variability reflects the mapped lithologic and hydrothermal changes thus identifying hydrothermal boundaries.

The expert-centered method is not without limitations. It is inherently subjective, since different experts may define morphologic classes differently, leading to epistemic uncertainty arising from differences in expertise, background, or mapping philosophy (Salisbury et al., 2015; Scharer et al., 2014; Adam et al., 2025). Nonetheless, this potential limitation is mitigated by the fact that the morphologic variability metric emphasizes relative change in form along the scarp, which remains robust for a given expert, even if absolute class definitions vary between experts. To reduce epistemic uncertainty, it is important that the expert explicitly state the field observations, the geometric framework, and the geologic reasoning in which the classification is grounded.

These strengths and limitations highlight the tradeoffs between interpretability and automation. While more advanced models, such as CNNs (Gao et al., 2021), CNN–transformer hybrid architectures (Li et al., 2025), or large-scale foundation models like GeomorPM (Yang et al., 2025) and U-ViT (Jiang et al., 2025), excel in automation and scalability, they can function as black boxes and lack discipline-specific interpretability. They also require extensive training data and are often not generalizable to different scenarios, introducing difficulties in data-poor areas. Even geospatial foundation models, which show strong generalization and few-shot learning across geospatial domains (Zhang et al., 2024), remain challenged by interpretability and adaptation to highly local, complex terrains. Ultimately, our method provides an interpretable, adaptable, and geologically grounded approach, ideal for environments like Dixie Valley where lithologic variability is critical, and training data are limited to a single, small, high-resolution topographic dataset. Our approach complements emerging foundation models and may, in future workflows, provide both validation data and interpretable signals for guiding AI-driven geomorphic analyses.

The sensitivity of our results to area selection within each unit merits discussion. Area A was selected as a baseline: a scarp in alluvial/colluvial material with known models of diffusion-based erosion (e.g., Wallace (1977); Bucknam and Anderson (1979); Nash (1980); Hanks (2000)). Areas B and C were defined based on mappable lithologic distinctions (silicified materials and hydrothermally altered materials, respectively). We deliberately avoided areas affected by alluvial fans or dissected by smaller channels to isolate the influence of material properties. The morphologic variability metric is designed to detect relative changes along the scarp, so the absolute boundaries matter less than capturing representative sections of each lithology. If the entire 600 m of scarp were analyzed as a single unit, the method would still detect variability changes, but the lithologic associations would be less clear. Future applications might analyze entire scarps continuously and use changes in the variability metric to identify previously unknown lithologic or structural boundaries.

Conclusions

Fault zones influenced by hydrothermal processes undergo mineralization, dissolution, and alteration, producing measurable contrasts in material properties that leave a lasting geomorphic imprint. The fault scarps we analyzed that were affected by hydrothermal activity exhibit distinct morphologic characteristics compared to those in unaltered gravels. The scarps affected by fumarolic activity produced low morphologic variability values by homogenizing the surface through chemical alteration that enabled rapid erosion, while high-temperature hot spring systems lead to increased variability through episodic cementation. The scarps in unaltered alluvium and colluvium maintained morphologies consistent with established conceptual models, providing a baseline against which the effects of hydrothermal alteration are measured.

The shape-based variability metric captures these differences, providing a novel and remote means of identifying hydrothermal zones along faults. The method does not require a priori assumptions about surface processes, allowing for greater flexibility and compatibility with machine learning classification techniques. On the other hand, the geologist-informed classification algorithm yields morphological classes that are interpretable in a geological context. The approach is effective in geologically complex regions even where training data are sparse, as we demonstrate using only a single high-resolution topographic dataset. Our results highlight the potential of fault scarp morphology as a proxy for surface and near surface hydrothermal alteration, offering new tools for structural mapping, geothermal exploration, and paleoseismology.

Acknowledgements

The authors thank Mark Coolbaugh for graciously sharing unpublished maps and field observations. Emma

Heitmann and Emma Sullivan provided valuable field assistance.

Land Recognition

The fieldwork was completed within areas of cultural significance to Northern Paiute and Western Shoshone tribes.

Data and Codes Availability

Code for calculating morphologic variability is openly available at https://github.com/Cassandra-Brigham/MorphologicVariability and archived at Zenodo: Brigham, C. A. P., Callahan, O. A., Crider, J. G. (2026). MorphologicVariability (v0.1.0) [Software]. Zenodo: https://doi.org/10.5281/zenodo.20128799. Field and thermal sUAS mapping of hydrothermal features, Section 10/15 Fumaroles, Stillwater Seismic Gap, Dixie Valley, NV. Includes descriptions of field and sUAS mapping campaigns conducted in 2022 and 2025, DSM and orthorectified thermal mosaics as rasters, and temperature control points as shapefiles. Material available in Zenodo repository: https://doi.org/10.5281/zenodo.16884014

Funding Statement

CAPB was supported by an NSF Graduate Research Fellowship and the David A.

Johnston Fellowship from the Department of Earth Sciences at the University of Washington and by NSF EAR 2040716 to OAC and JGC.

Fieldwork was partially supported by a grant to OAC from the Quaternary Research Center at the University of Washington.

Conflict of Interest Disclosure

The authors declare no competing interests.

Declaration on Artificial Intelligence Use

Machine learning is a central research tool in this study. Our approach is described in the methods section and in Brigham and Crider (2022). The authors declare that no artificial intelligence tool was used to assist in or generate the images or text of the manuscript.

References

Adam, R. N., Scott, C., Arrowsmith, J. R., et al. A systematic approach to mapping tectonic faults and documenting supporting geomorphology. *Geosphere*, 21(2):227–244, 2025. doi: 10.1130/GES02767.1.

Andrews, D. J. and Bucknam, R. C. Fitting degradation of shoreline scarps by a nonlinear diffusion model. *Journal of Geophysical Research: Solid Earth*, 92(B12):12857–12867, 1987. doi: 10.1029/JB092iB12p12857.

Andrews, D. J. and Hanks, T. C. Scarp degraded by linear diffusion: Inverse solution for age. *Journal of Geophysical Research: Solid Earth*, 90(B12):10193–10208, 1985. doi: 10.1029/JB090iB12p10193.

Avouac, J. P. Analysis of scarp profiles: Evaluation of errors in morphologic dating. *Journal of Geophysical Research: Solid Earth*, 98(B4):6745–6754, 1993. doi: 10.1029/92JB01962.

Backeberg, N. R., Rowe, C. D., and Barshi, N. Alteration-weakening leading to localized deformation in a damage aureole adjacent to a dormant shear zone. *Journal of Structural Geology*, 90: 144–156, 2016. doi: 10.1016/j.jsg.2016.07.008.

Bell, J. W. Quaternary Fault Map of the Reno 1° x 2° Quadrangle. Technical report, U.S. Geological Survey, 1981.

Bell, J. W. and Katzer, T. Timing of late Quaternary faulting in the 1954 Dixie Valley earthquake area, central Nevada. *Geology*, 18(7):622–625, 1990. doi: 10.1130/0091-7613(1990)018<0622:TOLQFI>2.3.CO;2.

Brigham, C. A. P. and Crider, J. G. A new metric for morphologic variability using landform shape classification via supervised machine learning. *Geomorphology*, 399:108065, 2022. doi: 10.1016/j.geomorph.2021.108065.

Browne, P. R. L. and Lawless, J. V. Characteristics of hydrothermal eruptions, with examples from New Zealand and elsewhere. *Earth-Science Reviews*, 52(4):299–331, 2001. doi: 10.1016/S0012-8252(00)00030-1.

Bucknam, R. C. and Anderson, R. E. Estimation of fault-scarp ages from a scarp-height–slope-angle relationship. *Geology*, 7(1):11–14, 1979. doi: 10.1130/0091-7613(1979)7<11:EOFAFA>2.0.CO;2.

Caine, J. S., Bruhn, R. L., and Forster, C. B. Internal structure, fault rocks, and inferences regarding deformation, fluid flow, and mineralization in the seismogenic Stillwater normal fault, Dixie Valley, Nevada. *Journal of Structural Geology*, 32(11): 1576–1589, 2010. doi: 10.1016/j.jsg.2010.03.004.

Callahan, O., Brigham, C., Heitmann, E., et al. High-resolution structure-from-motion models of hydrothermal sites in the Central Nevada Seismic Belt: applications in tectonic, climate, and hydrothermal investigations. In *Proceedings*, 2023.

Callahan, O. A., Eichhubl, P., Olson, J. E., and Davatzes, N. C. Fracture Mechanical Properties of Damaged and Hydrothermally Altered Rocks, Dixie Valley-Stillwater Fault Zone, Nevada, USA. *Journal of Geophysical Research: Solid Earth*, 124(4):4069–4090, 2019. doi: 10.1029/2018JB016708.

Callahan, O. A., Eichhubl, P., and Davatzes, N. C. Mineral precipitation as a mechanism of fault core growth. *Journal of Structural Geology*, 140:104156, 2020. doi: 10.1016/j.jsg.2020.104156.

Caskey, J. *Historic Faulting, Chronostratigraphy, and Paleoseismicity of the Central Nevada Seismic Belt: Field Guide*. 2002.

Chen, Z., Scott, C., Keating, D., Clarke, A., Das, J., and Arrowsmith, R. Quantifying and analysing rock trait distributions of rocky fault scarps using deep learning. *Earth Surface Processes and Landforms*, 48(6):1234–1250, 2023. doi: 10.1002/esp.5545.

Culling, W. E. H. Analytical Theory of Erosion. *The Journal of Geology*, 68(3):336–344, 1960.

Culling, W. E. H. Soil Creep and the Development of Hillside Slopes. *The Journal of Geology*, 71(2):127–161, 1963.

Freski, Y. R., Hecker, C., van der Meijde, M., and Setianto, A. The effects of alteration degree, moisture and temperature on laser return intensity for mapping geothermal manifestations. *Geothermics*, 97:102250, 2021. doi: 10.1016/j.geothermics.2021.102250.

Gao, B., Chen, N., Blaschke, T., et al. Automated Characterization of Yardangs Using Deep Convolutional Neural Networks. *Remote*

Sensing, 13(4):4, 2021. doi: 10.3390/rs13040733.

Hanks, T. C. The age of scarplike landforms from diffusion-equation analysis. In *Quaternary Geochronology: Methods and Applications*, volume 4, pages 313–338. American Geophysical Union, 2000. doi: 10.1029/RF004p0313.

Hanks, T. C., Bucknam, R. C., Lajoie, K. R., and Wallace, R. Modification of wave-cut and faulting-controlled landforms. *Journal of Geophysical Research: Solid Earth*, 89(B7):5771–5790, 1984. doi: 10.1029/JB089iB07p05771.

Heap, M. J., Kennedy, B. M., Pernin, N., et al. Mechanical behaviour and failure modes in the Whakaari (White Island volcano) hydrothermal system, New Zealand. *Journal of Volcanology and Geothermal Research*, 295:26–42, 2015. doi: 10.1016/j.jvolgeores.2015.02.012.

Hermant, B., Kiersnowski, L., and Bellanger, M. Using Deep Learning to Map Quaternary Faults in Western USA. In *Proceedings*, 2025.

Hodge, M., Biggs, J., Fagereng, Å., Elliott, A., Mdala, H., and Mphepo, F. A semi-automated algorithm to quantify scarp morphology (SPARTA): application to normal faults in southern Malawi. *Solid Earth*, 10(1):27–57, 2019. doi: 10.5194/se-10-27-2019.

Jiang, D., Li, S., Hajnsek, I., Siddique, M. A., Hong, W., and Wu, Y. Glacial lake mapping using remote sensing Geo-Foundation Model. *International Journal of Applied Earth Observation and Geoinformation*, 136:104371, 2025. doi: 10.1016/j.jag.2025.104371.

Juliani, C. Automated discrimination of fault scarps along an Arctic mid-ocean ridge using neural networks. *Computers & Geosciences*, 124:27–36, 2019. doi: 10.1016/j.cageo.2018.12.010.

Kennedy-Bowdoin, T., Martini, B. A., Silver, E. A., and Pickles, W. L. Hydrothermal Alteration Mineral Mapping Using Hyperspectral Imagery in Dixie Valley, Nevada. In *GRC Transactions*, volume 27, pages 649–651, 2003.

Kraal, K. O. and Schwering, P. C. Remote Sensing Case Studies for Detection and Interpretation of Geothermal Surface Materials for Geothermal Exploration in the Basin and Range, Nevada, USA. In *GRC Transactions*, volume 48, 2024.

Li, J., Zhang, J., and Fu, Y. CTHNet: A CNN–Transformer Hybrid Network for Landslide Identification in Loess Plateau Regions Using High-Resolution Remote Sensing Images. *Sensors*, 25(1):1, 2025. doi: 10.3390/s25010273.

Lutz, S. J., Caskey, S. J., and Johnson, S. D. Geyserite, Faulted Sinter Terraces, and Other Fossil Hot Spring Deposits, Northern Dixie Valley Fault System, Nevada. In *Geothermal Resources Council Transactions*, pages 75–89. 2003.

Lutz, S. S., Caskey, S. J., Mildenhall, D. D., Browne, P. R. L., and Johnson, S. D. Dating sinter deposits in northern Dixie Valley, Nevada - the paleoseismic record and implications for the Dixie Valley geothermal system. In *Proceedings*, page 10, 2002.

Martini, B. A., Silver, E. A., Pickles, W. L., and Cocks, P. A. Hyperspectral mineral mapping in support of geothermal exploration: examples from Long Valley Caldera, CA and Dixie Valley, NV, USA. In *Proceedings*, page 7, 2004.

Nash, D. B. Morphologic Dating of Degraded Normal Fault Scarps. *The Journal of Geology*, 88(3):353–360, 1980.

Pelletier, J. D., DeLong, S. B., Al-Suwaidi, A. H., et al. Evolution of the Bonneville shoreline scarp in west-central Utah: Comparison of scarp-analysis methods and implications for the diffusion model of hillslope evolution. *Geomorphology*, 74(1):257–270, 2006. doi: 10.1016/j.geomorph.2005.08.008.

Pereira, M. L., Zanon, V., Fernandes, I., Pappalardo, L., and Viveiros, F. Hydrothermal alteration and physical and mechanical properties of rocks in a volcanic environment: A review. *Earth-Science Reviews*, 252:104754, 2024. doi: 10.1016/j.earscirev.2024.104754.

Pierce, K. L. and Colman, S. M. Effect of height and orientation (microclimate) on geomorphic degradation rates and processes, late-glacial terrace scarps in central Idaho. *Geological Society of America Bulletin*, 97(7):869, 1986. doi: 10.1130/0016-7606(1986)97<869:EOHAOM>2.0.CO;2.

Pola, A., Crosta, G. B., Fusi, N., and Castellanza, R. General characterization of the mechanical behaviour of different volcanic rocks with respect to alteration. *Engineering Geology*, 169:1–13, 2014. doi: 10.1016/j.enggeo.2013.11.011.

Rahmidiani, W., Saepuloh, A., and Kriswati, E. Identification of Alteration Zones Based on Satellite Images and Vegetation Response for Geothermal Exploration in Volcanic Fields. *IOP Conference Series: Earth and Environmental Science*, 1451(1): 012033, 2025. doi: 10.1088/1755-1315/1451/1/012033.

Reid, M. E., Sisson, T. W., and Brien, D. L. Volcano collapse promoted by hydrothermal alteration and edifice shape, Mount Rainier, Washington. *Geology*, 29(9):779, 2001. doi: 10.1130/0091-7613(2001)029<0779:VCPBHA>2.0.CO;2.

Salisbury, J. B., Haddad, D. E., Rockwell, T., et al. Validation of meter-scale surface faulting offset measurements from high-resolution topographic data. *Geosphere*, 11(6):1884–1901, 2015. doi: 10.1130/GES01197.1.

Sare, R., Hilley, G. L., and DeLong, S. B. Regional-Scale Detection of Fault Scarps and Other Tectonic Landforms: Examples From Northern California. *Journal of Geophysical Research: Solid Earth*, 124(1):1016–1035, 2019. doi: 10.1029/2018JB016886.

Scharer, K. M., Salisbury, J. B., Arrowsmith, J. R., and Rockwell, T. K. Southern San Andreas Fault Evaluation Field Activity: Approaches to Measuring Small Geomorphic Offsets–Challenges and Recommendations for Active Fault Studies. *Seismological Research Letters*, 85(1):68–76, 2014. doi: 10.1785/0220130108.

Scott, C. P., Giampietro, T., Brigham, C., et al. Semiautomatic Algorithm to Map Tectonic Faults and Measure Scarp Height from Topography Applied to the Volcanic Tablelands and the Hurricane Fault, Western US. *Lithosphere*, 2021(Special 2):9031662, 2022. doi: 10.2113/2021/9031662.

Shebl, A., Abdellatif, M., Badawi, M., Dawoud, M., Fahil, A. S., and Csámer, . Towards better delineation of hydrothermal alterations via multi-sensor remote sensing and airborne geophysical data. *Scientific Reports*, 13(1):7406, 2023. doi: 10.1038/s41598-023-34531-y.

Thompson, G. A. and Burke, D. B. Rate and Direction of Spreading in Dixie Valley, Basin and Range Province, Nevada. *Geological Society of America Bulletin*, 84(2):627, 1973. doi: 10.1130/0016-7606(1973)84<627:RADOSI>2.0.CO;2.

Tucker, G. E. and Bradley, D. N. Trouble with diffusion: Reassessing hillslope erosion laws with a particle-based model. *Journal of Geophysical Research: Earth Surface*, 115(F1), 2010. doi: 10.1029/2009JF001264.

Tucker, G. E., McCoy, S. W., Whittaker, A. C., Roberts, G. P., Lancaster, S. T., and Phillips, R. Geomorphic significance of postglacial bedrock scarps on normal-fault footwalls. *Journal of Geophysical Research: Earth Surface*, 116(F1), 2011. doi: 10.1029/2010JF001861.

Van Der Meer, F., Hecker, C., Van Ruitenbeek, F., Van Der Werff, H., De Wijkerslooth, C., and Wechsler, C. Geologic remote sensing for geothermal exploration: A review. *International Journal of Applied Earth Observation and Geoinformation*, 33:255–269, 2014. doi: 10.1016/j.jag.2014.05.007.

Vega-Ramírez, L. A., Spelz, R. M., Negrete-Aranda, R., et al. A New Method for Fault-Scarp Detection Using Linear Discriminant

Analysis in High-Resolution Bathymetry Data From the Alarcón Rise and Pescadero Basin. *Tectonics*, 40(12):e2021TC006925, 2021. doi: 10.1029/2021TC006925.

Wallace, R. E. Profiles and ages of young fault scarps, north-central Nevada. *Geological Society of America Bulletin*, 88(9):1267, 1977. doi: 10.1130/0016-7606(1977)88<1267:PAAOYF>2.0.CO;2.

Wallace, R. E. and Whitney, R. A. Late quaternary history of the Stillwater seismic gap, Nevada. *Bulletin of the Seismological Society of America*, 74(1):301–314, 1984. doi: 10.1785/BSSA0740010301.

Wesnousky, S., Caskey, S. J., and Bell, J. W. Recency of Faulting and Neotechtonic Framework in the Dixie Valley Geothermal Field and Other Geothermal Fields of the Basin and Range. Technical report, University of Nevada, Reno (US), 2003.

Westoby, M. J., Brasington, J., Glasser, N. F., Hambrey, M. J., and Reynolds, J. M. 'Structure-from-Motion' photogrammetry: A low-cost, effective tool for geoscience applications. *Geomorphology*, 179:300–314, 2012. doi: 10.1016/j.geomorph.2012.08.021.

White, D. E. Violent mud-volcano eruption of Lake City Hot Springs, Northeastern California. *Geological Society of America Bulletin*, 66(9):1109–1130, 1955. doi: 10.1130/0016-7606(1955)66[1109:VMEOLC]2.0.CO;2.

Wintsch, R. P., Christoffersen, R., and Kronenberg, A. K. Fluid-rock reaction weakening of fault zones. *J. Geophys. Res.*, 100: 13021–13032, 1995. doi: 10.1029/94JB02622.

Wolfe, F. D., Stahl, T. A., Villamor, P., and Lukovic, B. Short communication: A semiautomated method for bulk fault slip analysis from topographic scarp profiles. *Earth Surface Dynamics*, 8(1): 211–219, 2020. doi: 10.5194/esurf-8-211-2020.

Wyering, L. D., Villeneuve, M. C., Wallis, I. C., Siratovich, P. A., Kennedy, B. M., Gravley, D. M., and Cant, J. L. Mechanical and physical properties of hydrothermally altered rocks, Taupo Volcanic Zone, New Zealand. *Journal of Volcanology and Geothermal Research*, 288:76–93, 2014. doi: 10.1016/j.jvolgeores.2014.10.008.

Xiong, L., Li, S., Tang, G., and Strobl, J. Geomorphometry and terrain analysis: data, methods, platforms and applications. *Earth-Science Reviews*, 233:104191, 2022. doi: 10.1016/j.earscirev.2022.104191.

Xu, J., Arrowsmith, J. R., Chen, J., et al. Evaluating young fluvial terrace riser degradation using a nonlinear transport model: Application to the Kongur Normal Fault in the Pamir, northwest China. *Earth Surface Processes and Landforms*, 46(1):280–295, 2021. doi: 10.1002/esp.5022.

Yang, J., Xu, J., Zhu, Y., Liu, Z., and Zhou, C. GeomorPM: a geomorphic pretrained model integrating convolution and Transformer architectures based on DEM data. *International Journal of Geographical Information Science*, 39(2):422–451, 2025. doi: 10.1080/13658816.2024.2414409.

Yellowstone Volcano Observatory. Yellowstone Volcano Observatory 2024 annual report. Technical Report 1566, U.S. Geological Survey, 2026.

Zhang, H., Xu, J. J., Cui, H. w., et al. When Geoscience Meets Foundation Models: Toward a general geoscience artificial intelligence system. *IEEE Geoscience and Remote Sensing Magazine*, pages 2–41, 2024. doi: 10.1109/MGRS.2024.3496478.

Zou, J., He, H., Yokoyama, Y., et al. A comparative study of bedrock fault scarps by s-UAV and t-LiDAR: Insights into site selection criteria for paleo-seismology studies. *Geomorphology*, 414: 108372, 2022. doi: 10.1016/j.geomorph.2022.108372.